remote sensing

MDPI

Article

Precision, Detection Limits, and Uncertainty in Multi-Temporal Geomatic Glacier Monitoring: The Rutor Glacier Case Study

Myrta Maria Macelloni [1,*], Fabio Giulio Tonolo [2], Vincenzo Di Pietra [1], Umberto Morra di Cella [3] and Alberto Cina [1]

[1] Department of Environment, Land and Infrastructure Engineering, Politecnico di Torino, 10129 Turin, Italy; vincenzo.dipietra@polito.it (V.D.P.); alberto.cina@polito.it (A.C.)
[2] Department of Architecture and Design, Politecnico di Torino, 10125 Turin, Italy; fabio.giuliotonolo@polito.it
[3] Climate Change Unit, Environmental Protection Agency of Valle d'Aosta, Loc. Grande Charrière, 48, 11020 Saint-Christophe, Italy; u.morradicella@arpa.vda.it
* Correspondence: myrta.macelloni@polito.it

Highlights

What are the main findings?

- A statistically robust framework based on DSM differencing and Limit of Detection (LoD) analysis enables reliable identification of actual glacier elevation changes.
- Spatially correlated uncertainty propagation improves the accuracy and reliability of glacier volume and mass-balance estimates derived from multi-temporal photogrammetric surveys.

What are the implications of the main findings?

- Explicit uncertainty quantification is essential to correctly interpret glacier changes and avoid misinterpretation caused by photogrammetric noise.
- The proposed methodology supports more reliable glacier monitoring and provides consistent geomatic products for climate-change studies and operational environmental analyses.

Abstract

Alpine glaciers are a vital resource for mountain regions. They provide water reserves, support energy production and tourism, and promote biodiversity. However, they are highly susceptible to climate change. In fact, they are recognised as being among the areas most affected by, and increasingly exposed to, natural hazards. The Rutor glacier in Aosta Valley, Italy, which has been the subject of repeated measurements since the 19th century and currently covers an area of around 8 km^2, is undergoing significant and continuous retreat. It thus serves as an exemplary case study of the impact of climate change on the Italian Alps. This ongoing research has made it possible to conduct multi-temporal analysis of the glacier. Within this framework, Politecnico di Torino, in collaboration with ARPA Valle d'Aosta, has developed a multidisciplinary research approach focused on the characterisation of alpine environments. This study illustrates the geomatic workflows and derived geospatial products that can be used to carry out a 4D monitoring of the extent and volume of the Rutor Glacier and estimate its mass balance over the past six years. A specific focus of the study is the propagation of errors in multi-temporal analyses used to quantify glacier melt, with particular attention to the precision of input 3D geospatial data and to the Limit of Detection of elevation differences, ultimately enabling the estimation of the uncertainty associated with the derived quantities and their temporal trends. Finally, advantages and limitations in the multi-temporal and multi-sensor monitoring of glaciers are presented and discussed.

Academic Editor: Ulrich Kamp

Received: 12 March 2026
Revised: 7 May 2026
Accepted: 10 May 2026
Published: 13 May 2026

Keywords: glacier retreat, drone/UAV; multi-temporal glacier monitoring; Limit of Detection;mass balance; DSM; photogrammetry

1. Introduction

Glaciers are significant indicators of climate change, often referred to as 'water towers' [1]. Reports from the Intergovernmental Panel on Climate Change (IPCC) [2,3] and recent assessments by the World Glacier Monitoring Service network (WGMS) [4] have shown that glaciers have been in constant decline. Since the mid-19th century, following their maximum extent during the final phase of the Little Ice Age, they have been retreating, leading to increased exposure to natural hazards and sea-level rise [5,6]. Furthermore, changes in the amount and distribution of runoff affect entire territories, impacting water resources, power production, agricultural productivity, and tourism. Projection models from the IPCC predict a decline in snow cover and glacial volume over the century. According to the RCP8.5 scenario, glaciers in the European Alps could lose over 80% of their current mass by 2100, with many potentially disappearing entirely.

The evolution and survival of the glacial mass are governed by two fundamental factors: the amount of snowfall during the winter months and summer temperatures. The former shape the extent of the 'accumulation basin', characterised by snow persistence and volume increase, while the latter drives the 'ablation basin', characterised by ice exposure and volume reduction with the consequent retreat of the front. The two distinctive regions are divided by the imaginary line called the equilibrium line altitude (ELA), which, in its variations in altitude, symbolises a genuine equilibrium between inflows from snow accumulation through direct deposition, wind transport and avalanches, and outflows from melting [7,8]. Due to climate change, a continuous rise in ELA has been observed, resulting constant glacier ablation [9].

Glaciological studies began in Italy at the end of the 19th century and continued at the beginning of the 20th century with periodic monitoring of Italian glaciers by the Italian Glaciological Committee [10]. Thanks to their location in densely populated and accessible areas, Alpine glaciers have been the subject of research studies by the WGMS since the late 1800s. Following the Scandinavian example, a programme to estimate mass balances in the Alps was launched in the 1940s, which was systematised into a glacier inventory around the 1970s. Aerial photography and early satellite imagery were the first tools used to map the characteristics of Alpine glaciers, until the early 21st century when modern technologies such as Light Detection and Ranging (LiDAR), drones and high-resolution satellites became commonly used for monitoring mountainous areas in the Alps [11].

Nowadays, high resolution remote sensing sensors from different platforms are mainly used to monitor thickness, volume, flow rates and changes in snow and ice. The data acquired through these sensors are essential for estimating geodetic mass balance and assessing subsequent environmental impacts. Remote sensing tools are powerful methods to monitor cryosphere combining different sensors [12] or using a single one over time [13].

For all these reasons, alpine glaciers are under constant observation by various Italian institutions and research bodies. Specifically, the multidisciplinary GlacierLAB at Politecnico di Torino [14] employs innovative technologies in collaboration with the Valle d'Aosta Environmental Protection Agency (ARPA) to monitor key glaciers in the Western Alps, situated between the Piedmont and Valle d'Aosta regions.

Despite the growing use of geodetic methods for glacier monitoring, the integration of co-registration assessment, Difference of Digital Surface models analysis, Limit of Detection estimation, and spatially explicit uncertainty propagation into a consistent and operational

workflow remains limited. While several studies have addressed these components individually (e.g., [15,16]), a gap persists in providing a unified pipeline that is both statistically rigorous and applicable to high-resolution photogrammetric products.

The present study aims to develop and apply a coherent multi-temporal framework for the quantification of glacier volume change and its associated uncertainty using photogrammetric Digital Surface Models (DSMs). The novelty of this work does not lie in the development of new individual methods, but in the integration of established approaches into a unified rigorous workflow that ensures methodological consistency and reproducibility. The proposed framework is applied to the Rutor Glacier based on geomatic techniques, highlighting the potential of high-resolution digital surface models for investigating glacier evolution. Although the framework is developed and tested on an Alpine glacier, its methodological structure is general and can be extended to other glaciated regions, including large and heterogeneous mountain systems such as High Mountain Asia (HMA). However, the applicability of the approach is also influenced by the operational constraints of the acquisition platforms, which may limit data acquisition in high-altitude environments and impose trade-offs between spatial resolution and coverage. The analysis framework supports the assessment of surface elevation changes and their uncertainties and provides a basis for glaciological applications such as the interpretation of equilibrium-line altitude variability, mass balance evolution (conducted by ARPA Valle d'Aosta), and volumetric changes.

2. Case Study

2.1. Site Description

The Rutor Glacier is located on the border between Italy and France in the Graian Alps, within the municipality of La Thuile (AO) as shown in (Figure 1). It ranks as the third-largest glacier in the Aosta Valley and is among the ten largest in the Italian Alps. The glacier covers an area of around 8 km^2 from its upper part at the Testa del Rutor peak (3486 m above mean sea level) to its lower margins (2550 m above mean sea level). It is bordered to the east by the Doravidi group, Tsassè Blanc, Flambeau, and Invergneures glaciers, and to the west by the Grande Assaly Glacier, while its upper reaches integrate the Saint Grat Dessus and Moriond Dessus basins.

As visible in the right Figure 1, the Rutor is a valley-type glacier complex composed of several accumulation basins. A prominent rocky outcrop known as 'Vedrette du Rutor' divides the system into two sectors, ultimately feeding three distinct glacial tongues at the terminus. The glacier is distinguished by a moderately steep central segment, characterised by a high prevalence of crevasses and a relatively smooth slope in the lower regions. This segment culminates in three distinct tongues (example of the east tongue in Figure 2a) that extend into the periglacial area. The upper reaches comprise extensive firn basins, currently investigated through multidisciplinary approaches [17]. It also forms three waterfalls that can be seen along the path that climbs from 'La Joux' to the Deffeyes mountain hut (Figure 2b).

Systematic monitoring by the Italian Glaciological Committee began at the end of the 19th century. The glacier reached its maximum historical extent during the Little Ice Age (LIA, 16th–19th centuries), when it extended to Lake Rutor. According to Villa et al. [18], the extension of LIA was approximately 12 km^2, reaching Lac du Glacier on the Plan del la Lierè plain above La Thuile. From the end of the LIA to 2004, the Rutor glacier underwent a frontal retreat of approximately 2 km, interrupted only by two periods of readvance characterised by low temperatures. Between the LIA and 1991, the glacier lost approximately 480 million cubic metres of ice and 34% of its surface area [17]. More recent morphological and volumetric analyses indicate that, in recent decades, mass loss has

predominantly occurred through surface lowering rather than frontal retreat, resulting in a general thinning while maintaining a relatively stable extent. Consistently, the equilibrium-line altitude (ELA) has risen from 2775 m a.s.l. during the LIA to 2850 m a.s.l. in 1991, corresponding to an increase of 75 m [18].

From the Middle Ages until the end of the LIA, the glacier was known for the floods caused by Lake Santa Margherita. The most destructive events recorded in the literature occurred between 1594 and 1598, with further episodes in the 17th century and notably in 1751 and 1752. During these periods the glacier covered the left bank of the basin, where it formed a lake of considerable size, preventing meltwater from flowing downhill. These floods, whose waters flowed into the Dora Baltea River, causing repeated and sometimes catastrophic events down to the valley floor; these events ended with the retreat of the glacier [19].

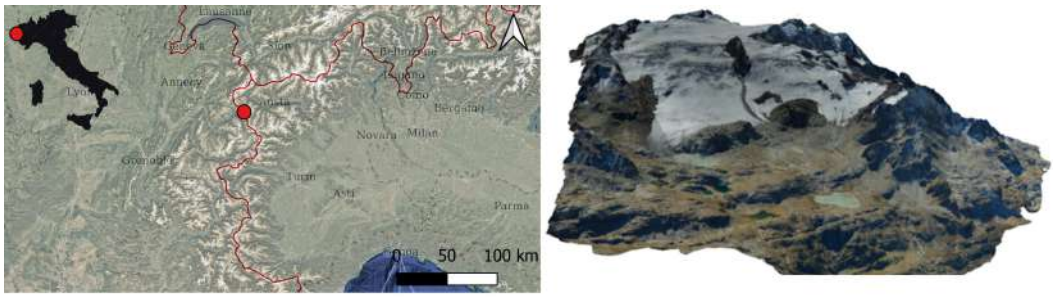

Figure 1. Rutor Glacier: territorial context of the study area (**left**) and three-dimensional view of the glacier (**right**).

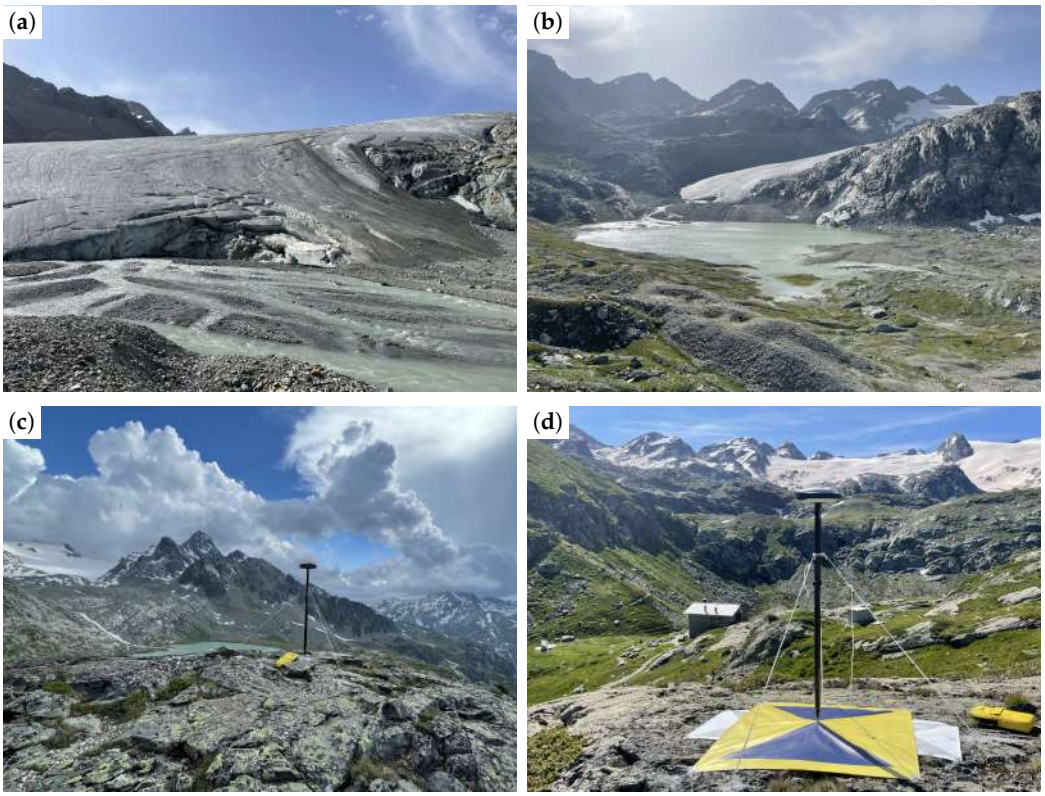

Figure 2. Rutor Glacier field campaigns: (**a**,**b**) east front overview from different perspectives during the 2023 campaign; (**c**) GNSS antenna and receiver installed on a control point for static precise positioning (Summer 2021); (**d**) one-metre by one-metre ground marker used in the glacier area.

2.2. Field Campaigns and Dataset

The GlacierLAB group has been conducting fieldwork on the Rutor Glacier since 2021. Every summer since July 2021, one or more measurement campaigns have been carried out in the glacial and periglacial areas of the glacier. During the field campaigns, a multidisciplinary team of researchers (e.g., hydraulics, geomatics, geophysics, etc.) travelled to the Rutor glacier area for extensive data acquisition campaigns [17,20]. The glacier's remote location presents significant logistical challenges, as it is accessible only by helicopter or via a demanding ascent on foot from La Joux, near La Thuile (AO, Italy).

This study focuses on the acquisition, processing and analysis of geomatics data from the glacier under examination.

The restricted accessibility required the optimisation of field equipment to minimise weight and logistical burden. To this end, the research team developed lightweight solutions, such as replacing traditional heavy tripods with compact adjustable anchors for GNSS (Global Navigation Satellite System) stations (Figure 2d). This adaptation allowed for greater mobility across the complex glacial terrain without compromising the precision of the ground control points.

In the first year (summer 2021), markers of different sizes were deployed: 0.50×0.50 m targets for UAV surveys and 1×1 m targets (Figure 2c) for aerial photogrammetric flights. Once positioned and fixed to the ground, the markers were named and measured with a GNSS receiver to determine their position with centimetric accuracy. The 3D coordinates of each target were measured with centimetric precision using Spectra Precision SP80 GNSS Receivers (Spectra Geospatial, Dayton, OH, USA), either in Real-Time Kinematic (RTK) mode by accessing the HxGN SmartNet GNSS correction service, where available, or using a local base–rover configuration with a master station installed at a barycentric point within the periglacier area.

Throughout the monitoring period (2020–2025) several DJI drone (SZ DJI Technology Co., Ltd, Shenzhen, China) surveys were conducted over the glacier front and periglacial zones using both RGB and multispectral sensors. A comprehensive summary of all geomatic measurement campaigns is provided in Table 1.

Table 1. Overview of field activities conducted on the Rutor Glacier. * In every campaign, there has been marker maintenance activity.

Year	Days	Activity
2021	8–10 July	Drone survey and placing marker
2021	19–21 July	Drone survey and placing marker
2021	6–8 September	Placing markers
2022	18–21 July	Drone survey *
2023	17–19 July	Drone survey *
2024	25 July	Drone survey and placing markers
2025	15–17 September	Drone survey *

Various sensors and platforms were used to monitor the medium-sized Rutor glacier. Within this multi-sensor framework, the analysis presented in this study focuses on aerial photogrammetric data to ensure consistency in spatial resolution and acquisition geometry across epochs. Accordingly, the main monitoring system is based on repeated aerial photogrammetric surveys covering the entire glacier. The survey was executed annually by a Tecnam P92 ultralight aircraft (Digisky, Turin, Italy). The aircraft was equipped with a PhaseOne 151.3 MP iXM-RS150F digital camera (Phase One Industrial, Frederiksberg, Denmark) (90 mm optics) medium format camera with a 50 mm focal length and a sensor

size of 40 mm × 53.5 mm. It was also equipped with a GNSS antenna and an inertial measurement unit (IMU) with metric accuracy.

The aerial photogrammetry flight was carried out every year from 2020 to 2025 in September. This timing coincides with the end of the hydrological year, when Alpine glaciers typically reach their minimum seasonal extent and snow cover is at its lowest before the onset of autumn snowfall. All flights took off from Turin using an unpressurized aircraft, maintaining a relative flight altitude of approximately 1000 m above ground level with a longitudinal and lateral overlap of 80%. Specifications for each aerial flight carried out on the Rutor glacier shows the flight altitudes, Ground Sample Distance (GSD) and number of Ground Control Points (GCPs), and Independent Check Points (ICPs) used for each aerial flight are reported in the Table 2.

Table 2. Summary of aerial photogrammetric surveys conducted on the Rutor Glacier.

Date	Hour	Avg. Flight Height [m]	GSD [m]	Area [km^2]	Images	GCPs	ICPs
30 September 2020	10:30–11:30	818	0.07	25.2	817	18	7
13 September 2021 and 30 September 2021	09:40–11:10 09:00–09:40	877	0.06	34.5	1100	9	4
10 September 2022	09:09–09:55	974	0.07	30.8	628	10	6
8 September 2023	10:52–11:46	1023	0.09	58.4	671	7	8
10 September 2024	11:30–12:21	1021	0.09	65.2	628	12	5
7 September 2025	15:12–16:00	1021	0.09	61.2	548	10	5

The periglacial area was also surveyed using DJI drones (e.g., Phantom 4, Mavic 3) on an annual basis during the measurement campaigns. These drone flights utilized RTK mode, referenced to a GNSS base station on points with known coordinates to ensure centimetric precision (Table 3).

Table 3. Summary of UAV survey acquisitions on the Rutor Glacier.

Date	UAV Type	GSD [m]	Area [km^2]	Number of Images
9 July 2021	DJI Phantom 4	0.03	2.61	1480
20 July 2021	DJI Phantom 4	0.03	1.48	991
18–19 July 2022	DJI Phantom 4	0.04	10.2	5268
18 July 2023	DJI Mavic 3	0.02	1.26	2310
25 July 2024	DJI Mavic 3	0.04	5.67	1753
16 July 2025	DJI Mavic 3	0.02	0.41	1072

For the multi-temporal analysis of glacier evolution, satellite data from multiple acquisition epochs were also processed. ARPA Valle d'Aosta provided the Glacier Lab of the Politecnico di Torino with a Pléiades stereo image pair acquired on 20 August 2017 at 10:34 UTC, with off-nadir viewing angles of ±8°. This acquisition resulted in an effective GSD of 0.71 m; the delivered products were resampled to 0.5 m by the data provider. The Pléiades sensor operates in the visible (VIS) and near-infrared (NIR) spectral ranges, with spatial resolutions of 0.7 m for the panchromatic band and 2.8 m for the multispectral bands, and a swath width of approximately 20 km at nadir. The imaged area covers 268.468 km^2 within the Aosta Valley region, near the borders with Piedmont and France, and includes several alpine sectors, such as the Gran Paradiso area and the Rutor Glacier.

A second very-high-resolution (VHR) Pléiades stereo image pair was acquired from the Pléiades-1A platform on 11 September 2022 at 10:23 UTC. The acquisition was characterised by a mean off-nadir angle of 23° and covered an area of 211.873 km^2 across the Italy–France

border. Similar to the 2017 dataset, the imagery includes VIS and NIR bands with a 0.7 m panchromatic GSD. All the satellite data are summarised in Table 4.

Table 4. Summary of satellite stereo acquisitions used in the study.

Date	Hour	Area [km^2]	Number of Images
20 August 2017	10:34	268.468	2
11 September 2022	10:23	211.873	2

To maintain methodological consistency in terms of spatial resolution and level of detail (Figure 3a), themulti-temporal analysis presented in this study focuses exclusively on the aerial photogrammetric datasets. Consequently, the UAV and satellite data, while integral to the broader monitoring project, are not the primary focus of this manuscript. Detailed analyses involving UAV and satellite platforms can be found in previous publications [21,22].

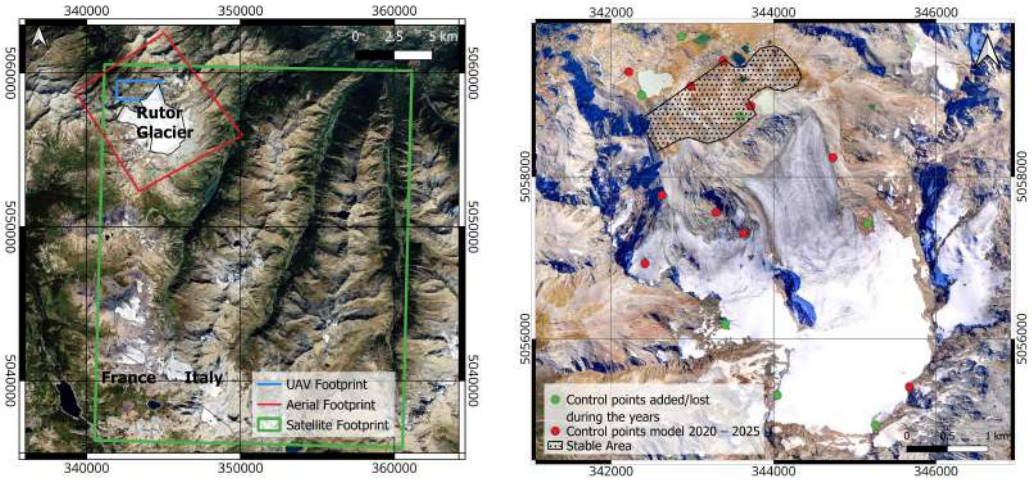

(**a**) Different footprint of cartographic products (**b**) Control Points and stable area

Figure 3. Overview of cartographic footprints and distribution of control points and stable areas. (RDN2008/UTM32N EPSG:6707).

3. Methods

This section outlines the methodological framework adopted to process the photogrammetric data, validate the derived products, perform multi-temporal comparisons, and quantify glacier elevation changes, associated uncertainties, and mass balance.

3.1. Aerial Photogrammetric Processing

The aerial photogrammetric data from each year were processed using Agisoft Metashape Professional version 2.2.1 software, following a consistent and standardized workflow.

Firstly, the acquired images are analysed to assess whether any of them need to be excluded from the processing (e.g., due to excessive cloud cover).

For the internal and relative orientation the images, the software identifies common geometries between images, i.e., it extracts feature points from which homologous points are detected through feature matching. Using the Structure from Motion (SfM) process, the position and orientation of the camera are determined, and the self-calibration parameters are estimated. The tie-point cloud is then generated. Given the large number of images, this step can take a considerable amount of time (up to 15 h processing with Intel(R) Core(TM) i9-9900X CPU @ 3.50 GHz, 8 GB VRAM NVIDIA QUADRO RTX4000, Santa

Clara, CA, USA). Targets with known coordinates are searched for and manually collimated on the images to carry out the external orientation, i.e., georeferencing the model, and optimise the internal camera parameters. The markers placed during field activities were used both as GCPs to assess the precision of the point cloud and as ICPs to estimate the positional accuracy. The spatial configuration along the glacier of control points over the years is shown in Figure 3b. The 3D models were all referenced in the ETRF2000/UTM32N coordinate system. Ellipsoidal elevations were converted to orthometric heights required for operational applications using the Italian geoid model ITALGEO05 with ConveRgo desktop software (Coordinate conversions for Regions) ensuring a conversion accuracy on the order of a few centimetres. After manually checking and refining the tie point cloud, a dense, colourful, high-resolution point cloud is generated using multi-view stereo matching (MVS) algorithms. At this point, cartographic products such as orthophotos and DSMs are generated and extracted.

The cartographic products obtained were evaluated and compared with each other for different purposes. First, the accuracy of the various products was examined in order to understand the common characteristics to assess their quality in terms of accuracy and precision.

Subsequently, multi-temporal comparisons were performed to quantify annual glacier ablation and cumulative changes over the entire 2020–2025 period. These derived products provided the basis for estimating the annual mass balance and monitoring the retreat of the glacial tongues.

3.2. DSMs: Validation, Difference of DSMs and Limit of Detection

Digital Surface Models derived from photogrammetric and remote sensing techniques are essential for quantifying changes in glacier surface elevation and volume. However, they inherently contain measurement errors related to image acquisition geometry, control point quality, and surface characteristics (such as snow cover, debris, and low-texture areas) that affect image matching performance. For this reason, a rigorous statistical assessment is required before DSMs can be reliably used for quantitative change detection and mass balance estimation.

To this end, we performed a multi-step validation to assess individual DSM accuracy, define the Limit of Detection (LoD) of their differences, and quantify the uncertainty associated with volumetric change estimates.

The adopted methodology follows a sequential approach:

1. Internal Validation: first, the accuracy of individual DSMs is evaluated using GCPs and ICPs;
2. Spatially Explicit Uncertainty: second, spatially distributed uncertainties are analysed through Differences of DSMs (DoDs) computed over stable areas;
3. LoD Determination: finally, these results are combined to derive the LoD at a defined confidence level. The entire methodological framework is schematically represented in Figure 4.

3.2.1. ICP Analysis

The first level of accuracy assessment focuses on the evaluation of single DSMs using ICPs. These are ground-surveyed points not included in the photogrammetric orientation or bundle adjustment. By computing the residuals between measured and modelled coordinates at ICP locations, the absolute accuracy of each DSM can be independently assessed.

In challenging glaciers and periglacial environments, the materialisation and spatial distribution of ICPs is particularly demanding, requiring significant logistical effort,

specialised personnel, and extensive fieldwork. Moreover, identifying points that remain invariant over time is often difficult. Nevertheless, even with a limited number of ICPs, it is possible to statistically evaluate DSM accuracy by computing the mean residual μ_z, which indicates potential systematic vertical biases, and the standard deviation σ_z, which quantifies the random component of vertical uncertainty. The same statistical indicators are also computed for the horizontal residuals x and y, as significant planimetric biases would indirectly affect vertical precision.

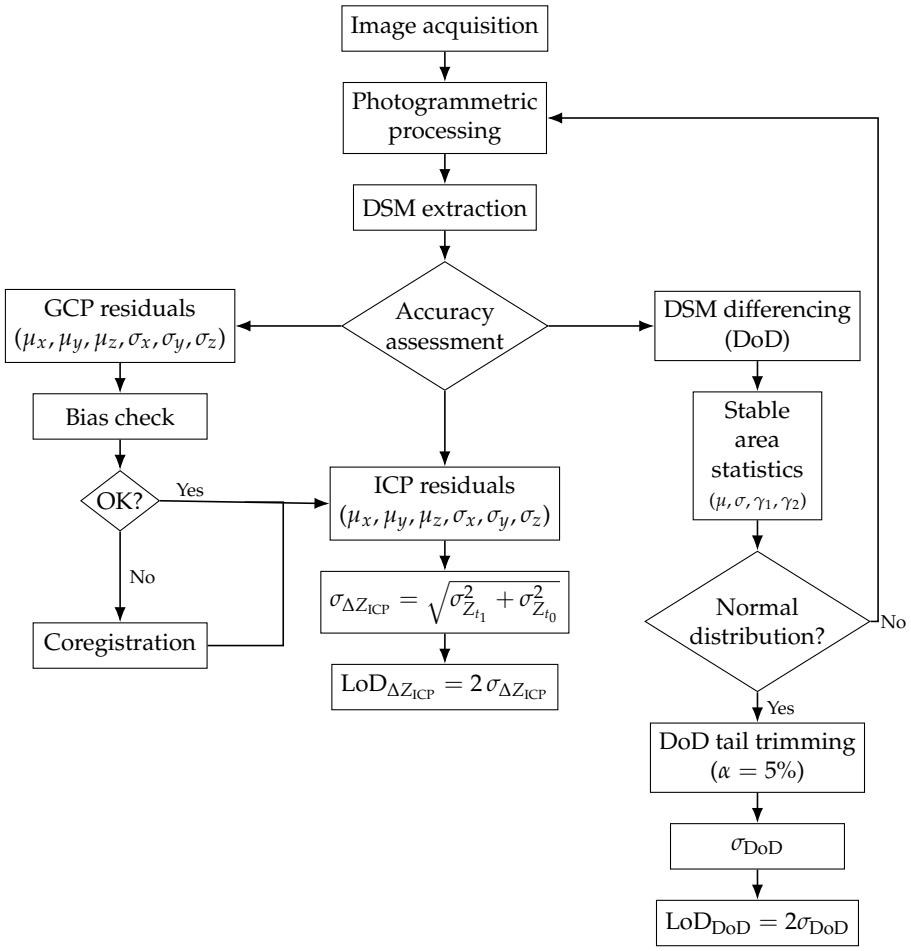

Figure 4. Integrated workflow for the multi-temporal DSMs comparison.

From a methodological perspective, the detection of significant planimetric biases would require corrective actions prior to any vertical change analysis. Systematic horizontal offsets or rotations can propagate into elevation differences, particularly in steep terrain, and should therefore be addressed through model re-orientation or co-registration procedures.

When the mean residuals are negligible compared to the standard deviation, particularly for the z component, which isex pected to be centred around zero, it indicates the absence of significant systematic vertical bias. While these points are suitable for internal validation of individual models, they are not sufficient on their own to robustly assess interannual DSM consistency and change detection. Any detected bias should be corrected prior to the estimation of the LoD; the procedure is described in Section 3.2.3

3.2.2. DoD Analysis

As a second validation method, DSMs from consecutive years are compared through DoDs, focusing exclusively on areas assumed to be stable over time. In a glacial context, stable areas typically correspond to rocky areas, consolidated moraines far from the active

glacier front, and other surfaces not affected by glacial or nival processes during the observation period. Due to the limited availability of surfaces that can be confidently considered stable, the extent of such areas is necessarily restricted and cannot be expanded without introducing potential bias.

Unlike the ICP-based approach, which relies on a limited number of point measurements, the DoD analysis exploits millions of elevation differences distributed over the study area, providing a more statistically robust assessment of uncertainty, though not strictly independent from the original measurements. This allows for the identification of residual biases, noise levels, and potential artefacts affecting the elevation change estimates.

The normality of the distribution, required for bias analysis, is evaluated using Fisher's skewness (γ_1) and kurtosis (γ_2) indices. For a theoretical Gaussian distribution, both indices are expected to approach zero. These are calculated as:

$$\gamma_1 = \frac{m_3}{m_2^{3/2}}, \tag{1}$$

$$\gamma_2 = \frac{m_4}{m_2^2} - 3; \tag{2}$$

where m_2, m_3, and m_4 are the second, third, and fourth central moments of the distribution, respectively, defined as $m_k = \frac{1}{n}\sum_{i=1}^{n}(x_i - \bar{x})^k$, with $\bar{x}$ denoting the sample mean and n the number of observations. To assess the proximity to zero, the z-values (normalized against their standard errors) can be tested under the null hypothesis that γ and γ_2 are equal to zero:

$$z_1 = \frac{\gamma}{\sqrt{6/n}}, \quad z_2 = \frac{\gamma_2}{\sqrt{24/n}} \tag{3}$$

To improve statistical robustness and mitigate the influence of gross outliers, often stemming from matching failures in photogrammetric processing, the distribution tails are trimmed by excluding the upper and lower 5% of the values. This threshold aligns with established practices in robust statistics [23] and common cartographic quality control, representing a practical compromise to remove gross errors without compromising the dataset's integrity.

A sensitivity analysis was performed to explicitly test the robustness of the adopted assumptions and evaluate the impact of different trimming levels (2% to 10%). The results show that the central tendency (trimmed mean and median) remains stable, while the standard deviation decreases progressively as noise is reduced. The adoption of a 5% trimming is thus a balanced and conservative choice. This analysis was carried out on the largest dataset (2020–2025), which includes approximately 4.5×10^6 points, ensuring statistical robustness.

These tests allow evaluating whether the adopted 5% trimming and Gaussian assumption represent robust methodological choices or if the results are influenced by these parameters.

3.2.3. LoD Analysis

The LoD defines the minimum elevation change that can be confidently distinguished from measurement noise when comparing DSMs acquired at different epochs. Assuming normally distributed errors, the LoD at the 95% confidence level is commonly defined as twice the standard deviation of the elevation differences [24–27].

For both processes (ICP and DoD) under the assumption of normal distribution, considering two epoch t_0 and t_1 and the coordinate K = $\{X, Y, Z\}$:

$$\mu_{\Delta K} = \text{mean}(\Delta K) \tag{4}$$

$$\sigma_{\Delta Z_{\mathrm{ICP}}} = \sqrt{\sigma^2_{Z_{t_1}} + \sigma^2_{Z_{t_0}}} \tag{5}$$

$$\mathrm{LoD}_{\Delta Z_{\mathrm{ICP}}} = 2\,\sigma_{\Delta Z_{\mathrm{ICP}}} \tag{6}$$

Similarly, for the DoD-based approach, the LoD is derived from the propagated uncertainty of the DSMs involved:

$$\mathrm{LoD}_{\mathrm{DoD}} = 2\,\sigma_{\mathrm{DoD}} \tag{7}$$

Elevation changes smaller than the LoD are considered statistically insignificant and are excluded from further interpretation. This filtering prevents noise-induced fluctuations from being misinterpreted as real surface changes and ensures that only statistically meaningful elevation differences contribute to volume and mass balance calculations.

The sequential application of ICP-based validation, DoD statistical analysis over stable terrain, and LoD estimation establishes a consistent framework for uncertainty quantification in multi-temporal DSM analyses. After tail trimming, DoD values computed over stable areas exhibit near-Gaussian behaviour, with mean values close to zero and limited dispersion. This supports the statistical validity of the adopted methodology and provides a solid basis for defining the LoD and propagating elevation uncertainties into volumetric change estimates for the Rutor Glacier. Such a robust approach is fundamental for enhancing the reliability of glacier elevation and volume change assessments in long-term monitoring and climate change impact studies.

3.3. Glacier Mass Balance

The mass balance (MB) of a glacier is defined as the net change in its mass over a given period, resulting from the difference between the accumulation of snow deposited during the winter season through solid precipitation and ablation due to snowmelt, sublimation and avalanches:

$$MB = P - M \tag{8}$$

where P is precipitation and M is the melted snow;

According to the WGMS, the direct historical method uses field measurements to first measure the accumulation at the end of winter. This is typically done through surveys and measurements of snow density, which allow the conversion of snow depth into water equivalent (w.e.). Then, by measuring ablation using ablation gauges inserted into the ice, the amount of ice that has melted is measured and converted using the density of ice. The local balance is then calculated and integrated on the glacier according to altitude [28].

Alternatively, the geodetic mass balance is derived from the volumetric variation between two epochs using multi-temporal DSMs:

$$\sum_{v,j}^{m,n} \Delta z_{i,j} = (\mathrm{DSM}_{t_1} - \mathrm{DSM}_{t_0}) \tag{9}$$

where Δz is the height difference between the two epochs and i, j is the DSM pixel. The total volume difference is calculated:

$$\Delta V = \int \Delta z \, \mathrm{d}A \tag{10}$$

where ΔV is the volume difference and A is the area of the glacier considered. Then the volume is converted into snow mass

$$\mathrm{MB} = \Delta V \cdot \rho_{\mathrm{ice/snow}} \tag{11}$$

where $\rho_{ice/snow}$ is the snow/ice density [26,29].

3.4. Impact of Altimetric Accuracy on Volumetric Estimation

Since glacier mass balance relies on converting volume change into mass change, any altimetric error propagates into uncertainty in the mass estimate. Furthermore, inaccuracies in glacier delineation can affect the estimated area and, consequently, the integrated volume change. As mentioned, the geodetic volume change was computed from the DoD as:

$$\Delta V = \sum_{i=1}^{N} \Delta z \, A_{pix} \tag{12}$$

where Δz is the elevation difference at pixel i, A_{pix} is the pixel area, and N is the number of valid pixels.

A first-order estimate assuming spatially uncorrelated elevation errors (e.g., [29]) would lead to unrealistically low uncertainties due to the large number of pixels involved. However, elevation errors in photogrammetric DSMs are typically spatially autocorrelated. To account for this, an effective number of independent observations, N_{eff}, was introduced following the conceptual framework of [16]. To be conservative, the correlation area A_c was approximated as a square with $2L$ side:

$$A_c \approx 4L^2, \tag{13}$$

where L is the characteristic correlation length of elevation errors.

To estimate L, the spatial structure of elevation errors was analysed over stable terrain DoD using the empirical variogram of the elevation differences. The empirical variogram was fitted using a spherical model:

$$\gamma(h) = \begin{cases} C_0 + C\left[\frac{3}{2}\left(\frac{h}{a}\right) - \frac{1}{2}\left(\frac{h}{a}\right)^3\right], & 0 \le h \le a, \\ C_0 + C, & h > a, \end{cases} \tag{14}$$

where C_0 is the nugget variance, C is the structured variance (sill minus nugget); $C_0 + C$ is the sill, h is the lag distance between pairs of points (two pixels) and a is the variogram range here adopted as the correlation length L.

The effective number of independent samples is then estimated as

$$N_{eff} = \frac{A}{A_c} \tag{15}$$

where A is the glacier area. The uncertainty of the volume change is finally computed as:

$$\sigma_V = A \, \frac{\sigma_{DoD}}{\sqrt{N_{eff}}} \tag{16}$$

where σ_{DoD} is the standard deviation of the DoD computed over the glacier area between the two epochs.

The spatially correlated elevation uncertainties described in glacier and geomorphological applications are computed following the approach of previous studies [16,26,27].

In order to explicitly link uncertainties to the final mass-balance estimates, the propagation of errors was considered, starting from the geodetic formulation (11). According to the variance propagation law, the total uncertainty σ^2_{MB} is estimated as:

$$\sigma^2_{MB} = (\rho \, \sigma_V)^2 + (\Delta V \, \sigma_\rho)^2 \tag{17}$$

where σ_V is the uncertainty in volume change derived from the DoD analysis and spatial correlation, and σ_ρ is the uncertainty associated with the density conversion factor. (typically ranging from 60 to 100 kg/m^3).

4. Results

4.1. Orthophotos and DSMs

Cartographic products for each year were extracted from the relevant models processed using the method described in Section 3.1. All annual datasets between 2020 and 2025 were exported as rasters with a GSD of 0.5 m to facilitate management and multitemporal comparison (Figure 5a,b). Figure 6 illustrates the relative level of detail provided by satellite, aerial, and UAV orthophotos, highlighting the superior resolution achieved through the platforms.

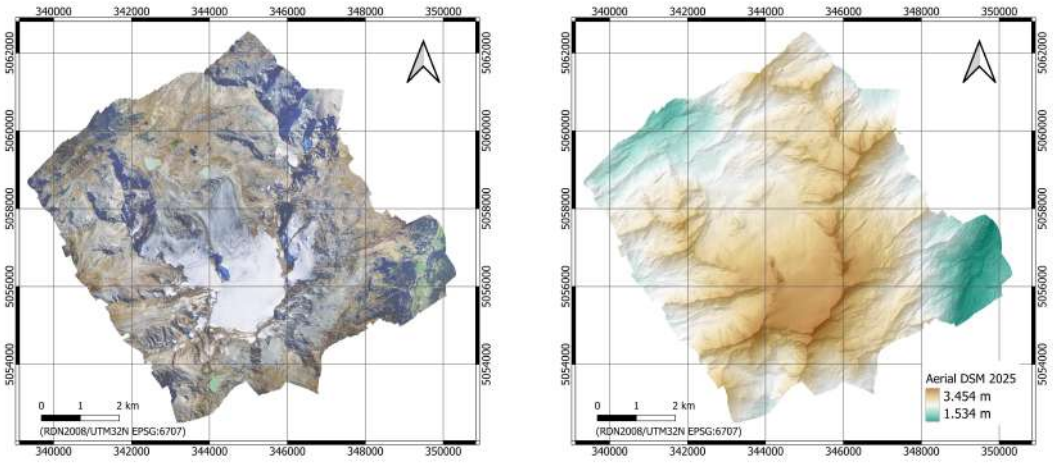

(**a**) Orthophoto of the Rutor Glacier (2025) (**b**) DSM of the Rutor Glacier (2025)

Figure 5. Orthophoto and digital surface model of the Rutor Glacier acquired in 2025. Reference system: RDN2008/UTM32N EPSG:6707.

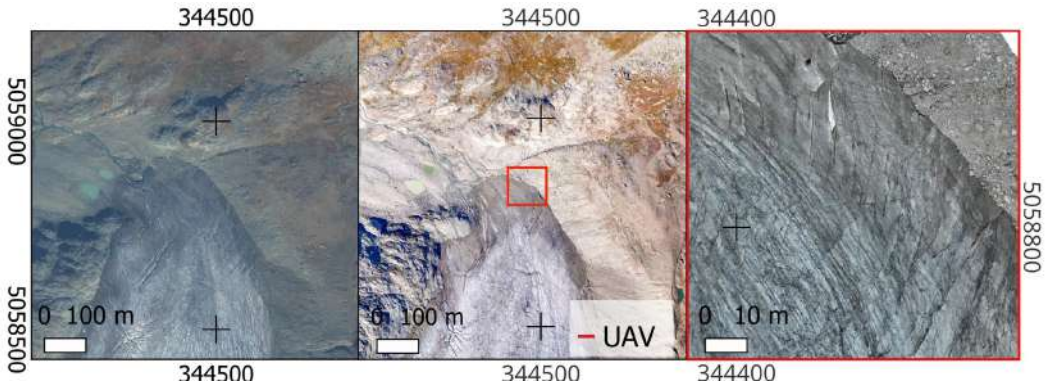

Figure 6. Level of detail of satellite, aerial, and UAV orthophoto, respectively. The red square highlights the area shown in detail in the UAV orthophoto. Reference system: RDN2008/UTM32N EPSG:6707.

The accuracy of each model was evaluated by analysing the residual errors at both GCPs and ICPs, as summarised in Table 5.

The residuals calculated on the GCPs show mean values very close to zero along all spatial components (μ_x, μ_y, μ_z), with average deviations generally within a few millimetres. Standard deviations are low, particularly for the planimetric components, indicating a high precision in the range of 0.10 m with 0.00 m min and 0.21 m max values. As expected in photogrammetric processes, the vertical component exhibits slightly higher dispersion;

however, the values remain consistent with the GSD of the data and with the expected survey accuracy.

Residuals computed on the ICPs show greater dispersion than those on the GCPs, especially along the vertical component. Nevertheless, mean residuals on ICPs remain close to zero, indicating the absence of significant systematic biases in the reconstructed models. Planimetric residuals are generally on the order of the pixel size, while vertical residuals are approximately twice the image resolution, which is consistent with typical photogrammetric accuracy ratios.

A noticeable decrease in the number of both GCPs and ICPs is observed for the 2025 model, mainly due to the deterioration or loss of several markers, which became missing or unusable as reference points. Over time, the spatial distribution of markers has changed: some have degraded, faded, or been physically removed, while others have been replaced or restored where possible. This aspect highlights the intrinsic difficulty of maintaining stable reference points in high-mountain environments. Despite these variations, the overall results in Table 5 indicate that the photogrammetric models maintain stable accuracy over time, providing a reliable foundation for multi-temporal analysis.

Table 5. Means and standard deviations of the residuals calculated on GCPs and ICPs.

			Residuals on GCPs [m]			**Residuals on ICPs [m]**		
Year	**GSD [m]**	**N. GCPs**	$\mu_x \pm \sigma_x$	$\mu_y \pm \sigma_y$	$\mu_z \pm \sigma_z$	$\mu_x \pm \sigma_x$	$\mu_y \pm \sigma_y$	$\mu_z \pm \sigma_z$
2020	0.5	18	0.01 ± 0.21	-0.00 ± 0.13	0.00 ± 0.11	-0.03 ± 0.20	0.10 ± 0.11	0.03 ± 0.18
2021	0.5	9	0.00 ± 0.04	0.00 ± 0.03	0.00 ± 0.06	-0.06 ± 0.05	-0.00 ± 0.01	0.04 ± 0.12
2022	0.5	10	0.00 ± 0.02	0.00 ± 0.00	0.00 ± 0.00	-0.08 ± 0.15	-0.08 ± 0.03	-0.08 ± 0.07
2023	0.5	8	0.00 ± 0.04	0.00 ± 0.05	0.01 ± 0.16	-0.02 ± 0.05	-0.00 ± 0.04	-0.08 ± 0.22
2024	0.5	12	0.00 ± 0.06	0.00 ± 0.08	0.00 ± 0.09	-0.06 ± 0.04	0.03 ± 0.08	-0.07 ± 0.12
2025	0.5	10	-0.00 ± 0.04	-0.00 ± 0.05	0.00 ± 0.13	-0.02 ± 0.03	0.06 ± 0.12	-0.15 ± 0.33

4.2. Statistical Analysis of Stable Areas and DoD Uncertainty

To implement the second validation approach, DoDs were generated for all possible year pairs over the Rutor Glacier. In order to estimate the accuracy of the DoDs, it was first necessary to identify areas that could be considered stable over time. To this purpose, Figure 7 shows the confidence map generated by Agisoft Metashape, highlighting a spatially variable reliability of the reconstructed points. Lower confidence values are mainly observed in the upper part of the glacier and along its margins, where image matching is affected by steep slopes, shadowing effects and unfavourable acquisition geometry. In addition, due to the complex orography of the area, surrounding ridges and lateral slopes and zones located above the glacier cannot be assumed to be invariant over time, as they may be affected by gravitational processes, rockfalls, and seasonal instabilities.

For these reasons, only the periglacial areas surrounding the glacier were selected as stable reference surfaces for the subsequent analyses. These zones provide more reliable and temporally consistent conditions and therefore represent the most suitable areas for the assessment of elevation differences and for the estimation of the uncertainty associated with the Difference of DSMs.

The statistical analysis on DoD described and applied on the stable area (4,754,665 points) of the Figure 7 is reported in the Table 6.

The statistical analysis performed on these stable areas (comprising approximately 4.5×10^6 points) is reported in Table 6. The skewness (γ_1) and excess kurtosis (γ_2) values indicate that the error distributions are approximately Gaussian, supporting the assumption that residual elevation differences are dominated by random noise rather than systematic shifts. For the 2020–2025 period, the raw distribution showed slight asymmetry ($\gamma_1 = 0.36$) and a flatter-than-normal shape ($\gamma_2 = -0.48$). To evaluate the robustness of our statistical

assumptions, a sensitivity analysis was performed. Figure 8 presents the Q–Q plot after a 5% tail trimming, showing that the central portion of the distribution closely follows the theoretical normal line. Deviations are restricted to the extreme quantiles, likely due to residual outliers and correlation mismatches. This confirms that, after trimming, the residuals can be reasonably approximated as Gaussian, a practice widely accepted in geodetic glacier studies [16,29].

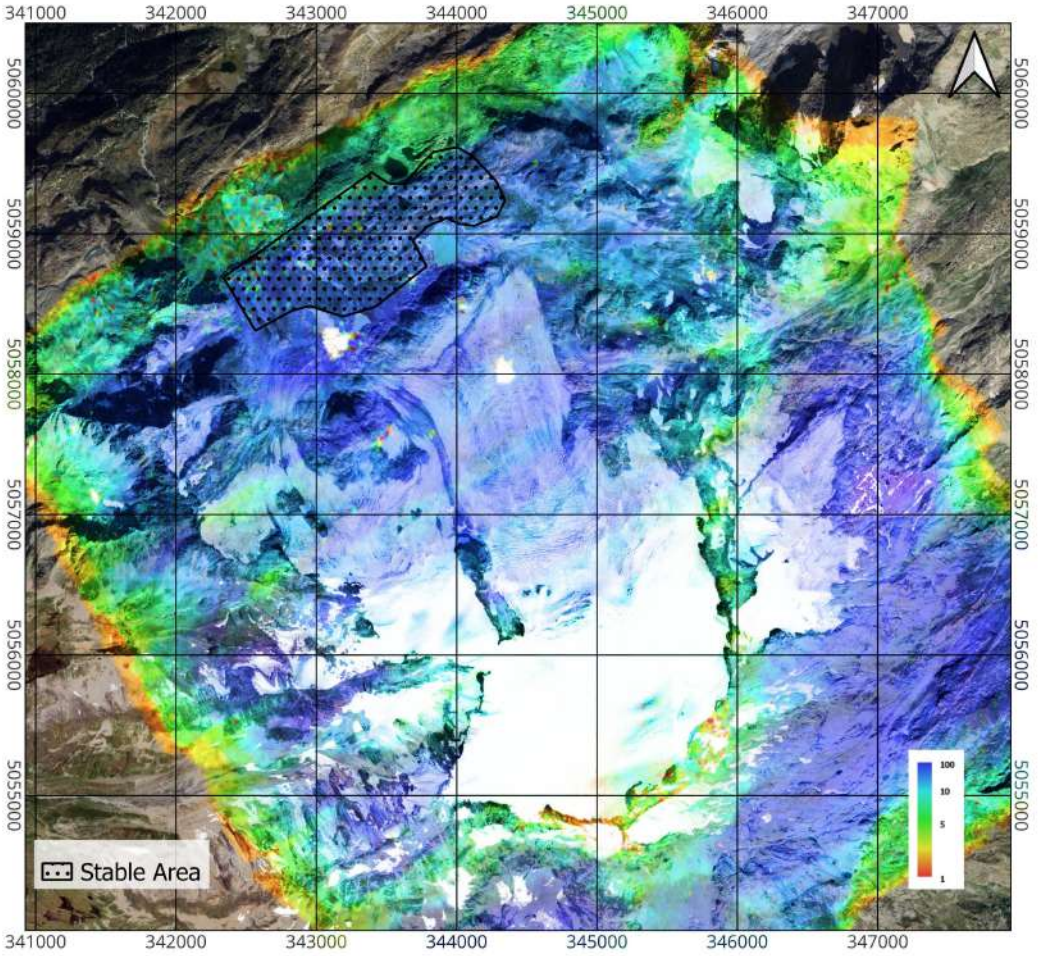

Figure 7. Confidence map of the Rutor Glacier derived from the photogrammetric reconstruction. The colour bar represents a dimensionless index of relative photogrammetric confidence. It highlights the spatial distribution of reconstruction reliability, where lower values (warm colours) correspond to areas with challenging geometry or poor image matching, such as steep slopes or shadows [30]. Reference system: RDN2008/UTM32N EPSG:6707.

Table 6. Statistics of DoD values computed over stable areas after removing outliers.

Years	Mean and Std. $\mu_{DoD} \pm \sigma_{DoD}$ [m]	Median [m]	Mean and Std. Without Tails (5%) $\mu_{DoD} \pm \sigma_{DoD}$ [m]	γ_1 Fisher	γ_2 Fisher
2021–2020	-0.03 ± 0.29	-0.08	-0.05 ± 0.17	0.78	0.11
2022–2021	-0.00 ± 0.14	-0.02	-0.01 ± 0.09	0.51	0.18
2023–2022	0.01 ± 0.19	0.02	0.01 ± 0.15	0.12	-0.82
2024–2023	0.02 ± 0.19	-0.00	0.01 ± 0.14	0.56	-0.45
2025–2024	0.02 ± 0.21	0.02	0.02 ± 0.15	0.20	-0.38
2025–2020	-0.00 ± 0.36	-0.05	-0.02 ± 0.26	0.36	-0.49

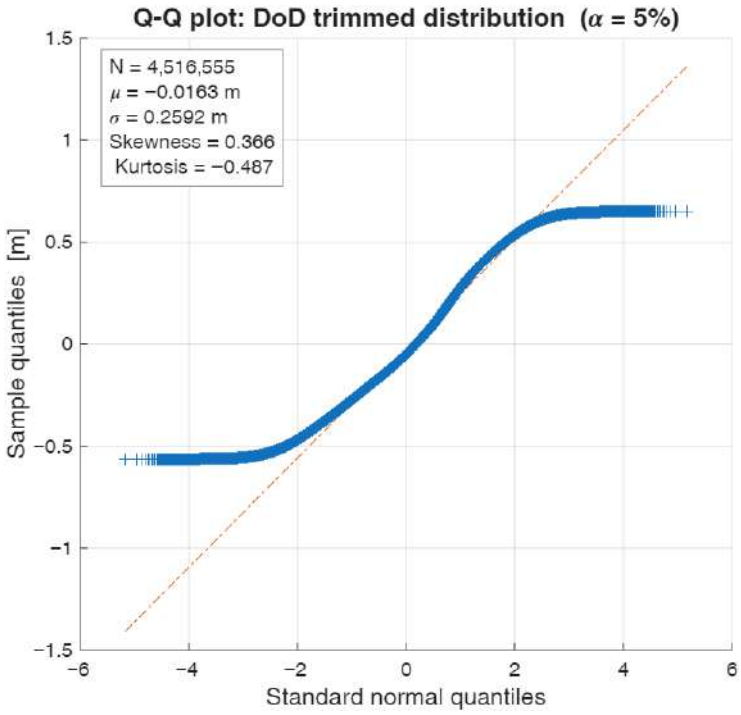

Figure 8. Q–Q plot of the DoD elevation differences over stable areas for the 2020–2025 period after applying a 5% tail trimming. The orange dashed line represents the theoretical normal distribution, while the blue markers represent the sample quantiles of the trimmed elevation differences.

The robustness of the trimming threshold was further assessed by varying the level between 2% and 10% (Figure 9). The trimmed mean and median remained nearly invariant (within a few millimeters), while the standard deviation decreased as expected with the removal of noise. Thus, the 5% trimming represents an optimal compromise between reducing outlier influence and preserving the dataset's statistical representativeness.

The comparison between the mean and standard deviation values computed before and after trimming shows that the DoD distributions are consistently centred around zero for all temporal pairs. This indicates the absence of significant systematic biases between the DSMs. Small variations in standard deviation among different years reflect changes in acquisition conditions, surface characteristics, and photogrammetric performance, but remain within a narrow and consistent range.

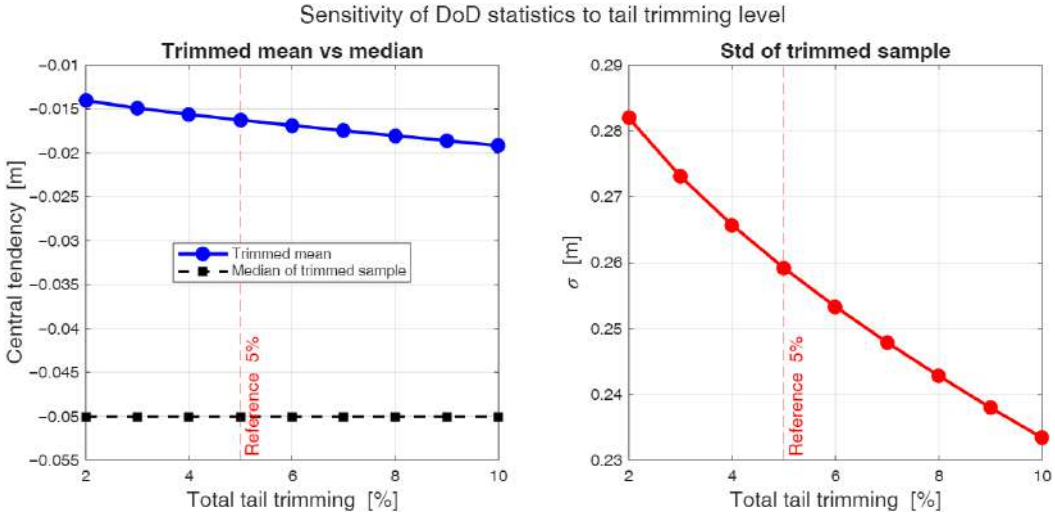

Figure 9. Sensitivity of DoD statistics to different tail trimming levels (2–10%). The vertical dashed line indicates the adopted 5% threshold.

4.3. Comparison of LoD Approaches

Table 7 reports the LoD values calculated for each DoD between subsequent epochs using two independent approaches. The second column shows the LoD derived from the ICPs, calculated using the σ_z values reported in Table 5 and following the methodology described in Section 3.2.3. The third column reports the LoD computed directly from the DoD statistics, obtained as twice the σ_{DoD} values reported in Table 6.

A clear difference emerges between the two approaches. The LoD derived from ICPs is systematically higher and, in most cases, approximately twice that obtained from the DoD analysis. This difference reflects the limitations of point-based assessments in complex terrains, where a small number of ICPs may be more sensitive to local conditions or positioning errors. Conversely, the DoD-based approach leverages a massive set of spatially distributed observations, capturing the actual noise characteristics of the elevation differences more effectively. Consequently, the DoD-based LoD is considered more appropriate for defining statistically significant elevation changes and was adopted for the subsequent volumetric calculations.

Table 7. Limit of Detection (LoD) computed without tails ($\alpha = 5\%$) for each DoD.

Years	$\mathbf{LoD}_{\Delta Z_{ICP}}$ [m]	$\mathbf{LoD}_{DoD}$ [m]
2021–2020	$2\sqrt{(0.18)^2 + (0.12)^2} = 0.43$	0.34
2022–2021	$2\sqrt{(0.12)^2 + (0.07)^2} = 0.27$	0.18
2023–2022	$2\sqrt{(0.07)^2 + (0.22)^2} = 0.46$	0.22
2024–2023	$2\sqrt{(0.22)^2 + (0.12)^2} = 0.50$	0.26
2025–2024	$2\sqrt{(0.12)^2 + (0.33)^2} = 0.70$	0.30
2025–2020	$2\sqrt{(0.18)^2 + (0.33)^2} = 0.75$	0.52

4.4. Glacier Surface Elevation Changes

Figure 10 shows the spatial distribution and interannual evolution of glacier surface lowering. Each panel represents the annual DoD between consecutive surveys, while the last map shows the cumulative elevation change over the 2020–2025 period, providing an integrated view of the glacier thinning. To enhance the visual interpretation of glacier melting patterns, different legend scales were adopted. In particular, the colour scale of the cumulative DoD (2020–2025) was intentionally amplified to better highlight long-term elevation changes. In order to standardise the visualisation and to adopt a conservative approach consistent with the uncertainty analysis, elevation differences within the uncertainty range of ±1 m were rendered transparent in the annual DoD maps. This threshold corresponds to the order of magnitude of the Limit of Detection derived from the DoD statistics for all years and prevents the visual interpretation of changes that are not statistically significant.

For the cumulative DoD over the entire period, the transparency threshold was increased to ±2 m for graphical purposes only, reflecting the accumulation of interannual uncertainties and allowing a clearer representation of the long-term elevation changes. This approach ensures a consistent and conservative visualisation of glacier thinning while preserving the comparability between annual and multi-annual DoD products.

As shown in Figure 11, the elevation differences on stable areas are consistently centered around zero, with average deviations limited to a few centimeters. The standard deviations range between 0.13 m and 0.26 m, representing roughly one-third of the GSD. This high level of alignment across the multi-temporal dataset ensures that the observed changes on the Rutor Glacier are physically meaningful and reflect actual ice loss rather than georeferencing artifacts.

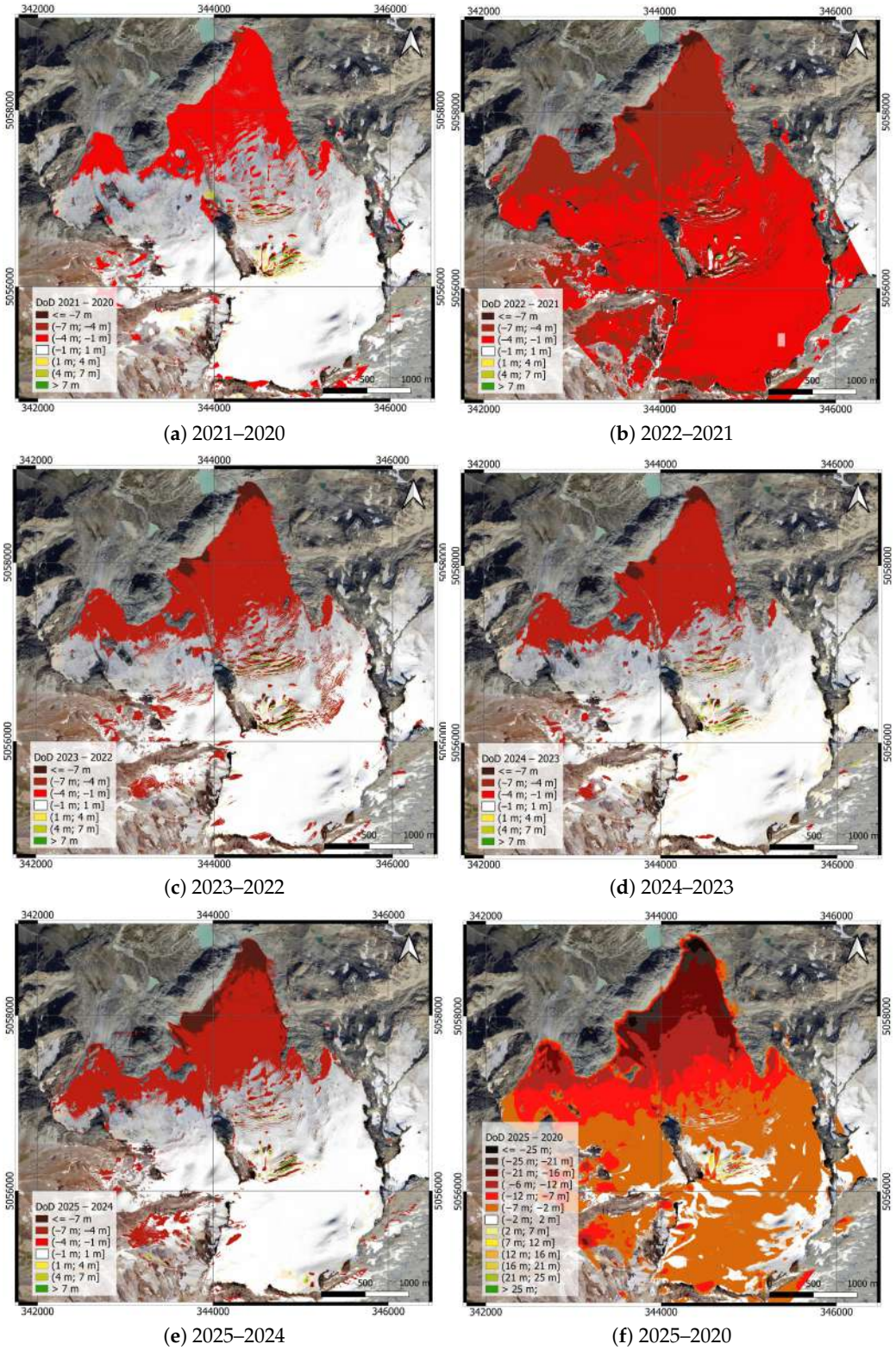

Figure 10. Difference of DSM (DoD) maps of the Rutor Glacier for the analysed periods between 2020 and 2025. Annual DoDs are shown for consecutive survey pairs, while the cumulative DoD for the entire 2020–2025 period is reported in the last panel and adopts different DoD color-ranges as shown in the legend. Reference system: RDN2008/UTM32N EPSG:6707.

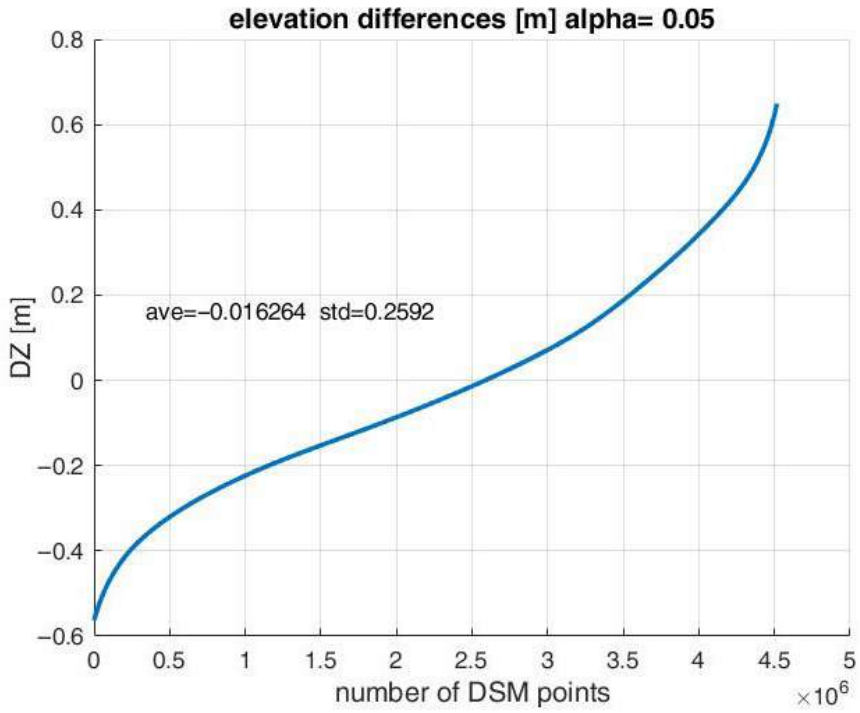

Figure 11. Statistics on 2020–2025 on DoDs stable areas.

5. Operational Applications

Glacier monitoring is essential for assessing the impacts of climate change on alpine environments, as well as for evaluating water resources and related natural hazards. In recent decades, geomatic surveys have become central to glacier research due to their ability to provide quantitative, repeatable, and high-resolution spatial information. Techniques such as aerial and satellite photogrammetry, optical remote sensing, and DSM processing enable detailed analyses of glacier extent, surface elevation, and volumetric changes across multiple spatial and temporal scales.

The integration of multi-sensor datasets acquired at different times allows glacier geometry and dynamics to be analysed within a consistent framework, supporting mass balance estimation and the interpretation of surface processes. Specifically,multi-temporal analysis based on the Difference of DSMs (DoD) [31] allows for the quantification of altimetric variations and glacial volume fluctuations [32]. This approach is widely used in glaciological studies as it enables the integration of spatially continuous observations with more precise field measurements. At the same time, high-resolution orthophotos enable the precise mapping of changes in glacier area, retreating fronts [33], the evolution of moraines and the appearance of debris surfaces or proglacial lakes [34]. The integration of DoDs and orthophotos within a coherent geomatic [35] framework is therefore an effective and well-established method for glacier monitoring, allowing for the synergistic analysis of planimetric and volumetric changes and supporting climatic, hydrological, and risk assessment studies in the Alpine environment. The following sections illustrate the application of these methodologies to the Rutor Glacier.

5.1. Multitemporal Glacier Monitoring

The repeated surveys conducted yearly, in addition to the historical products enable to estimate the reduction in thickness and the retreat of the lower part of the Rutor glacier. The eastern tongue is the part of the glacier most impacted, retreating and lowering each year significantly, mainly due to high summer temperatures. Although winter precipitation increases the albedo of the glacier and helps preserve it during winter, prolonged periods

of high summer temperatures significantly impact glacial melting, despite the glacier's high altitude. The lower part of the glacier, like the three tongues, has been characterised by noticeable thinning of around 4 metres per year (Figure 10) during the monitoring period. Peculiar condition were observed in 2022–2023, when a snowless winter combined with an exceptionally hot summer led to a significantly higher-than-average ablation rates, pushing the ELA to very high altitude. Moreover, by means of visual interpretation of the orthophotos (including data retrieved from historical archives) it was also possible to monitor the tongue outline evolution to estimate the average planimetric retreat of the glacier (Figure 12).

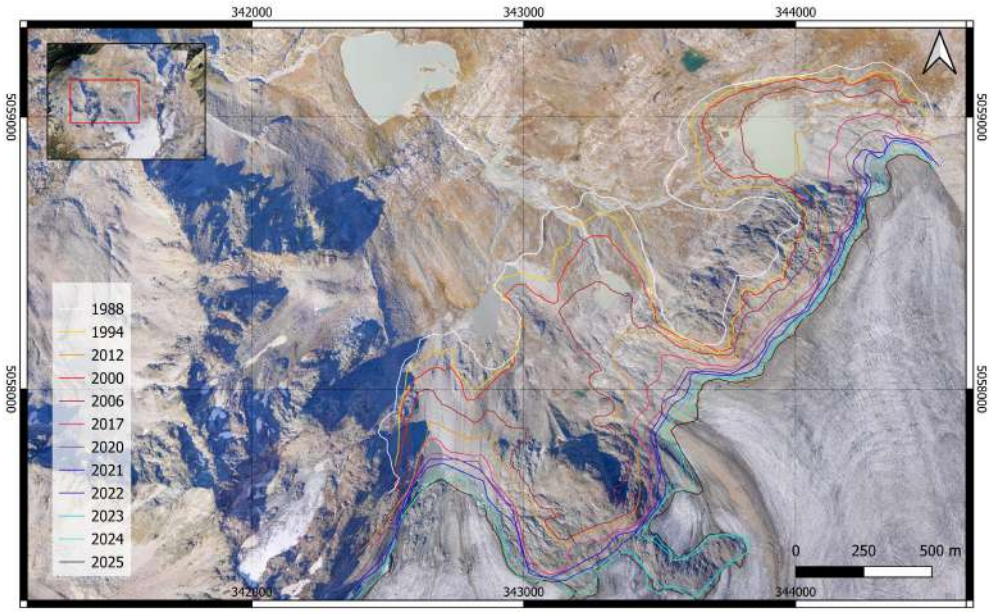

Figure 12. Glacier footprint during the period 1988–2025; historical data from Geoportale Nazionale [36] Reference system: (RDN2008/UTM32N EPSG:6707) The red rectangle in the inset map indicates the area shown in detail in the main figure.

5.2. Rutor Mass Balance Between 2020 and 2025

Regarding the Rutor glacier mass balance, the second approach described in Section 3.3 was used by Aosta Valley ARPA on the cartographic products obtained from the photogrammetric process. To convert volume changes into mass changes, a density value of $\rho = 850 \pm 60$ kg m^{-3} was adopted, following the recommendation of [37] for Alpine glaciers where both ice and firn melting contribute to volume loss.

Comparing the 2025 mass balance with those of recent years (2024: −506 mm w.e.; 2023: −1.010 mm w.e.; 2022: −3.867 mm w.e.) shows that, although all three years recorded negative values, the losses in 2025 were substantially less severe than in 2022. The 2025 and 2024 balances are comparable and considerably less negative than that of 2023, which reflects the impact of higher-than-average summer temperatures that enhanced melting. Overall, the measurements yield a net mass balance of −746 mm w.e. for the Rutor Glacier. Snow accumulation measurements carried out on the Rutor Glacier in May 2025 indicated values slightly above the 24-year average, though still lower than those recorded during the 2023–24 winter. By the end of the accumulation period, the mean snow depth across the glacier was 396 cm, equivalent to 1.955 mm of water, well above the 20-year mean (2005–2025) of 1.370 mm (Figure 13). On the right front (mean elevation 2635 m a.s.l.), the glacier surface thinned by an average of 4.5 m and retreated by approximately 25 m. On the plateau and central front (mean elevation 2725 m a.s.l.), the average surface lowering

was 3.6 m, with a retreat of around 15 m. Finally, the left front (mean elevation 2720 m a.s.l.) showed an average thinning of 2.6 m and a retreat of around 12 m [38], (Figure 14).

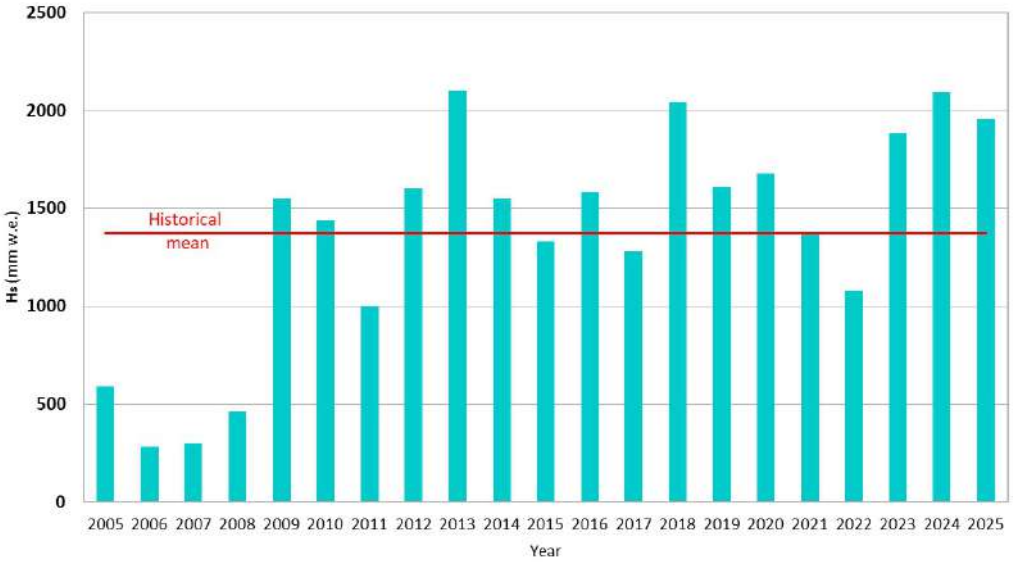

Figure 13. Historical series of accumulations at the Rutor Glacier. The average calculated over the 20 year series is shown in red. Reproduced with permission from ARPA VDA [38].

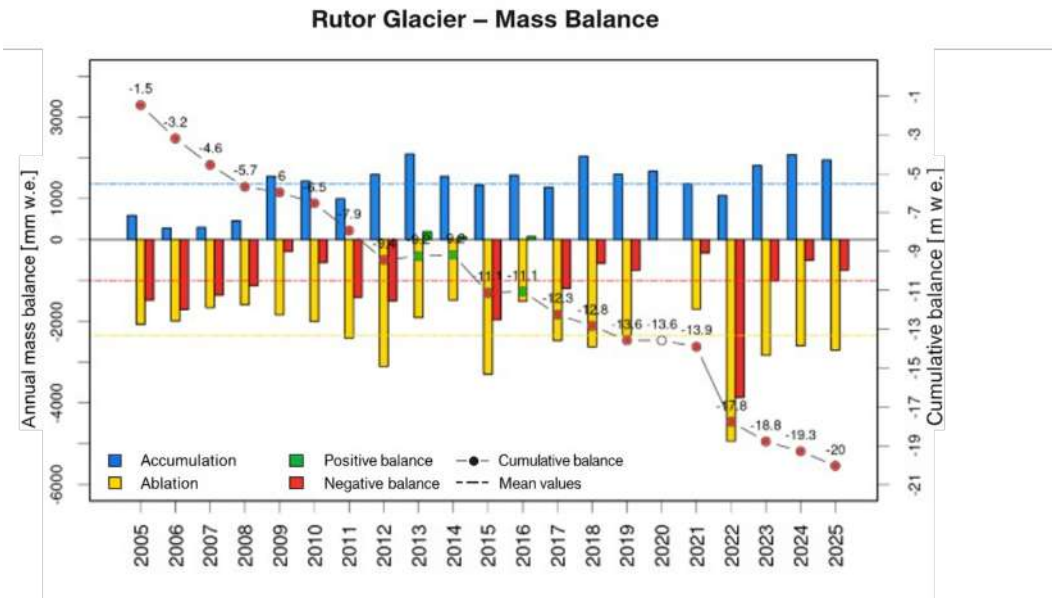

Figure 14. Mass balance of the Rutor Glacier during the observation period (2005–2025): slightly above-average snow accumulation did not protect the glacier from summer melting, leading to a more negative mass balance than in the previous season. Reproduced with permission from ARPA VDA [38].

5.3. Impact of Altimetric Accuracy on Volumetric Estimation on Rutor Glacier

The methodology described in Section 3.4 is applied to each epoch pair. Figure 15 shows the empirical variogram for the period 2020–2025, according to the spherical model, computed on the stable area considered.

The parameters estimated from the spherical variogram applied to stable-terrain DoDs are reported in Table 8. The spatial correlation length of elevation error (L) varies between 64 and 76 m, indicating a stable spatial autocorrelation pattern across survey campaigns. Moderate interannual variations of the nugget component (C_0) and the structured variance (C) likely reflect differences in acquisition conditions, such as imaging geometry. The sill

($C_0 + C$) values are comparable among epochs, implying a similar magnitude of elevation uncertainty.

Table 8. Spherical variogram parameters estimated from stable-terrain DoDs. L corresponds to the spherical range parameter.

$\mathbf{Year_{start}}$	$\mathbf{Year_{end}}$	L [m]	C_0 (Nugget)	C	Sill
2020	2021	76.000	0.0057173	0.0036966	0.0094139
2021	2022	72.571	0.0070219	0.0028595	0.0098814
2022	2023	76.000	0.0054306	0.0021077	0.0075383
2023	2024	76.000	0.0017661	0.0024283	0.0041944
2024	2025	64.120	0.0082965	0.0048158	0.0131120
2020	2025	64.555	0.0165550	0.0113520	0.0279070

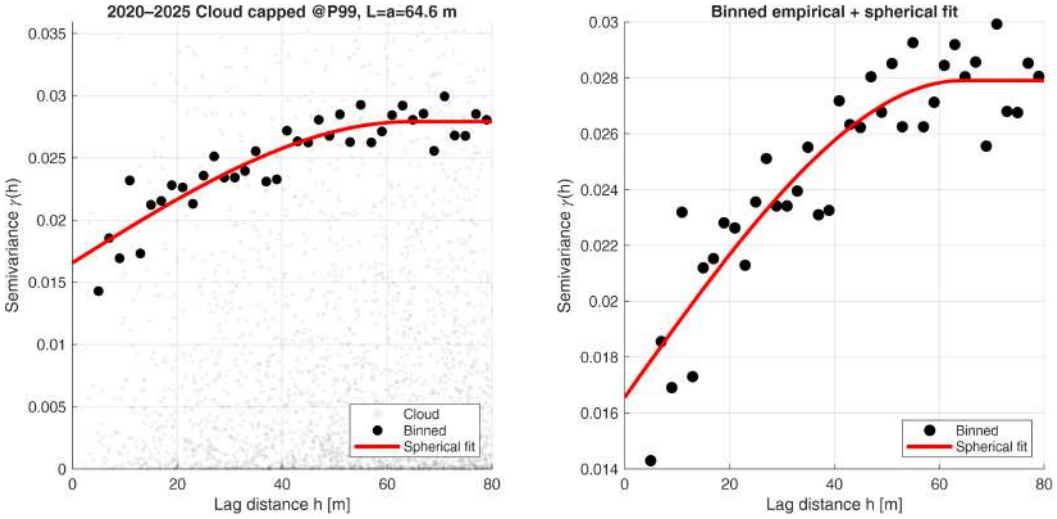

Figure 15. Empirical variogram of stable-terrain elevation differences for the 2020–2025 period. (**Left**) Variogram cloud based on randomly sampled point pairs (capped at the 99th percentile for visualisation), together with the binned empirical semivariance and the fitted spherical model. (**Right**) Binned empirical variogram and corresponding spherical fit. The estimated correlation length corresponds to the spherical range parameter ($L = a = 64.6$ m).

The derived correlation lengths directly influence the effective sample size (N_{eff}), thereby controlling the magnitude of the volumetric uncertainty (σ_V). As shown in Table 9, annual volume uncertainties range from approximately 0.06 to 0.18 Mm^3. For the cumulative 2020–2025 period, the correlation length of 64.56 m results in a total volume uncertainty of 3.35 Mm^3. These values provide a rigorous and realistic uncertainty bound, accounting for the spatial dependencies typical of photogrammetric products.

The Rutor Glacier exhibits persistent negative volume changes, with annual losses generally ranging between 3 and 8 Mm^3. The 2021–2022 hydrological year was exceptionally critical due to a dry winter followed by a prolonged, warm summer, resulting in substantially greater ablation than in subsequent years (Figure 16a). While the 2022–2023 and 2023–2024 periods show a relative reduction in loss, the trend remains negative, indicating continued glacier thinning. The cumulative volume loss over the 2020–2025 period, obtained by summing interannual changes, amounts to 56.29 Mm^3 (Figure 16a). This trend is dominated by the 2021–2022 extreme event, suggesting that single years of enhanced ablation can exert long-term control over multiannual glacier evolution. Relative uncertainties in annual volume change range from 0.2% to 5%, while the cumulative uncertainty is approximately 6%, confirming that the observed signal is consistently distinguishable from noise.

Table 9. Annual and cumulative glacier volume change and associated uncertainty based on variogram-derived correlation length. Mass balance in mm w.e. computed using $\rho = 850 \pm 60\,\mathrm{kg\,m^{-3}}$ [37].

Years	L [m]	A_c [m^2]	ΔV [Mm^3]	σ_V [Mm^3]	σ_V [%]	MB [mm w.e.]
2020–2021	76.00	23,104	−5.865	0.18339	3.13	-662 ± 51
2021–2022	72.57	21,066	−33.401	0.06411	0.19	-3770 ± 266
2022–2023	76.00	23,104	−6.619	0.08702	1.31	-747 ± 54
2023–2024	76.00	23,104	−2.595	0.11824	4.56	-293 ± 25
2024–2025	64.12	16,445	−7.802	0.08304	1.06	-881 ± 63
2020–2025	64.56	1.67×10^8	−56.281	3.351	5.96	-6353 ± 587

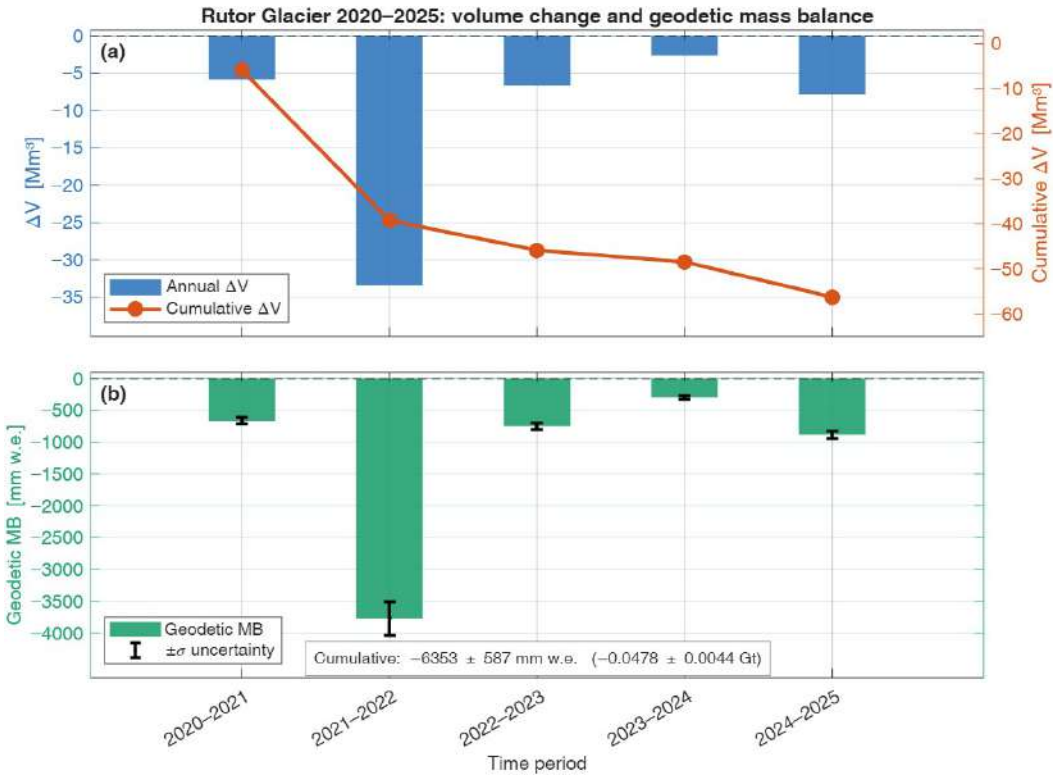

Figure 16. (**a**) Annual (bars) and cumulative (line) glacier volume change for the 2020–2025 period. (**b**) Annual geodetic mass balance with associated uncertainties ($\pm\sigma$), derived from volume change using $\rho = 850 \pm 60\,\mathrm{kg\,m^{-3}}$ [37].

To evaluate the geodetic mass balance, these volume changes were converted using the adopted density factor. The resulting annual mass balances (Figure 16b) confirm a robust negative signal. Uncertainties range between ±25 and ±266 mm w.e., remaining consistently below 10% of the observed losses. Even for the extreme 2021–2022 loss (−3770 mm w.e.), the signal-to-noise ratio remains high, ensuring that the detected changes are physically meaningful. The cumulative 2020–2025 mass balance of -6353 ± 587 mm w.e. provides a clear, quantitative measure of the ongoing rapid deglaciation of the Rutor massif, well-constrained beyond the limits of photogrammetric noise.

6. Discussion and Conclusions

This study demonstrates that multi-temporal aerial photogrammetry, when implemented through a consistent geomatic workflow, provides a robust basis for monitoring Alpine glaciers and deriving geodetic mass-balance estimates. The main contribution of this work does not lie in the introduction of new individual techniques, but in the integration of established approaches into a coherent and reproducible framework including

standardized photogrammetric processing, ICP-based validation, DoD analysis over stable periglacial areas, LoD definition, and spatially correlated uncertainty propagation. In this sense, the proposed workflow extends previous applications of photogrammetric glacier monitoring and geodetic mass-balance assessment [15,39] by explicitly linking product validation, change detection, and uncertainty quantification within a single operational sequence.

The Rutor Glacier represents a particularly demanding case study because of its large extent, complex topography, steep slopes, variable illumination conditions, and limited accessibility, all of which constrain both field operations and image acquisition geometry. In this context, the analysis of the photogrammetric confidence map proved essential for identifying sectors affected by shadowing, steep terrain, and unfavourable image geometry, and therefore for guiding the selection of stable periglacial areas used in the uncertainty assessment. Restricting the DoD statistics to these areas reduced the influence of poorly constrained sectors and improved the robustness of the derived detection limits and volume-change estimates.

The results also clarify the different roles of ICP-based and DoD-based validation. ICPs remain useful for the internal validation of individual DSMs and for detecting potential systematic biases, but their limited number and uneven spatial distribution make them insufficient, on their own, for robust multi-temporal comparison over large and heterogeneous alpine terrain. Conversely, the DoD-based approach, relying on spatially distributed stable areas, provides a more representative estimate of elevation-change uncertainty. This is particularly important when spatial autocorrelation is explicitly considered, as recommended in geodetic glacier studies [16]. The adoption of a spatially correlated uncertainty model allowed the propagated errors on volume and mass balance to remain realistic and prevented the severe underestimation that would arise from assuming pixel-wise independence.

From the results perspective, the Rutor Glacier exhibits persistent and spatially coherent thinning throughout the 2020–2025 period, despite marked interannual variability. All analysed intervals are characterised by predominantly negative elevation changes, while the 2021–2022 hydrological year stands out as the most critical phase, owing to substantially enhanced ablation. Although the magnitude and spatial distribution of annual losses vary from year to year, the cumulative DoD provides the clearest representation of glacier evolution and reveals a robust long-term negative signal. This behaviour is coherent with glacier retreat and mass-loss trends reported for the Italian Alps [40]. Over the full 2020–2025 period, the glacier lost 56.281 Mm^3 of ice volume, corresponding to a geodetic mass balance of -6353 ± 587 mm w.e., thus providing a well-constrained quantitative measure of ongoing rapid deglaciation.

Importantly, the uncertainty analysis strengthens rather than weakens the interpretation of these results. Stable-area DoDs remain centred close to zero, annual and cumulative changes exceed the corresponding detection limits, and the explicit treatment of spatial autocorrelation yields realistic uncertainty bounds for both volumetric and geodetic mass-balance estimates. The observed signal therefore remains clearly distinguishable from photogrammetric noise, even when conservative assumptions are adopted.

An additional source of uncertainty is related to glacier boundary delineation, particularly in debris-covered areas at the glacier terminus, where the distinction between ice and surrounding terrain relies on geomorphological interpretation of orthophotos and DSMs. While such uncertainty may locally affect volume estimates, its overall impact is limited by the relatively small spatial extent of these sectors compared to the entire glacier.

Beyond the specific case study, the operational value of the proposed approach lies in its ability to transform repeated geomatic surveys into uncertainty-aware products for

environmental monitoring. The integration of orthophotos, DoDs, volumetric estimates, and geodetic mass-balance products provides a spatially continuous and reproducible basis for assessing glacier evolution, hydrological implications, and related mountain hazards. In the present case, these geomatic products were also used by ARPA Valle d'Aosta to derive snow water equivalent and mass-balance indicators, showing the practical relevance of the proposed workflow for institutional monitoring activities.

Repeated annual surveys are essential not only for describing long-term trends, but also for capturing extreme years that can disproportionately control multiannual glacier evolution. Future developments should therefore focus on translating uncertainty-aware geomatic products into standardized operational outputs, such as annual indicators of glacier change, DoD maps explicitly filtered by detection limits, and cumulative time series of volume change and geodetic mass balance with associated uncertainty bounds. Such products would improve the comparability of multi-temporal surveys, facilitate communication with environmental agencies and decision makers, and strengthen the operational use of photogrammetric glacier monitoring for climate-impact assessment and glacier-risk management. Although the framework is demonstrated here on an Alpine glacier, its methodological structure is general and can be extended to other glaciated regions where repeated DSMs are available.

Author Contributions: Conceptualization, A.C., M.M.M. and F.G.T.; methodology, A.C., M.M.M. and F.G.T.; software, A.C. and M.M.M.; validation, A.C. and F.G.T.; formal analysis, A.C. and M.M.M.; investigation, A.C., M.M.M. and F.G.T.; resources, A.C.; data curation, M.M.M.; writing—original draft preparation, M.M.M.; writing—review and editing, A.C., F.G.T., V.D.P., M.M.M. and U.M.d.C.; visualization, M.M.M. (with contributions from all co-authors); supervision, A.C., F.G.T., V.D.P. and U.M.d.C.; project administration, A.C.; funding acquisition, A.C. All authors have read and agreed to the published version of the manuscript.

Funding: This research was supported by the Italian Ministry for Education and Research (MIUR) through the "Department of Excellence 2018–2022" programme awarded to the Department of Environment, Land and Infrastructure Engineering (DIATI) at the Politecnico di Torino. The funding contributed to the acquisition of part of the installed equipment and to the execution of crewed aerial photogrammetric flights.

Data Availability Statement: The data supporting the results reported in this study are publicly available on Zenodo at https://doi.org/10.5281/zenodo.19255342.

Acknowledgments: The authors thank Andrea Ajmar, Nives Grasso and Paolo Maschio for their support during the field campaigns, including field activities and logistical assistance.

Conflicts of Interest: The authors declare no conflicts of interest.

References

1. Immerzeel, W.W.; Lutz, A.F.; Andrade, M.; Bahl, A.; Biemans, H.; Bolch, T.; Hyde, S.; Brumby, S.; Davies, B.J.; Elmore, A.C.; et al. Importance and vulnerability of the world's water towers. *Nature* **2020**, *577*, 364–369. https://doi.org/10.1038/s41586-019-1822-y.
2. IPCC. *Climate Change 2021: The Physical Science Basis*; Cambridge University Press: Cambridge, UK, 2022. https://doi.org/10.1017/9781009157896.
3. IPCC. *Climate Change 2023: Synthesis Report*; Intergovernmental Panel on Climate Change: Geneva, Switzerland, 2023.
4. Zemp, M.; Welty, E.; Nussbaumer, S.U.; Bannwart, J.; Gärtner-Roer, I.; Wells, A.; Ahlstrøm, A.P.; Anderson, B.; Andreassen, L.M.; Azam, M.F.; et al. Global glacier mass change in 2025. *Nat. Rev. Earth Environ.* **2026**, *7*, 213–215. https://doi.org/10.1038/s43017-026-00777-z.
5. Reinthaler, J.; Paul, F. Reconstructed glacier area and volume changes in the European Alps since the Little Ice Age. *Cryosphere* **2025**, *19*, 753–767. https://doi.org/10.5194/tc-19-753-2025.
6. Carrivick, J.L.; Davies, M.; Wilson, R.; Davies, B.J.; Gribbin, T.; King, O.; Rabatel, A.; García, J.L.; Ely, J.C. Accelerating Glacier Area Loss Across the Andes Since the Little Ice Age. *Geophys. Res. Lett.* **2024**, *51*, e2024GL109154. https://doi.org/10.1029/2024GL109154.

7. Tielidze, L.G.; Mackintosh, A.N.; Gavashelishvili, A.; Gadrani, L.; Nadaraia, A.; Elashvili, M. Post-Little Ice Age Equilibrium-Line Altitude and Temperature Changes in the Greater Caucasus Based on Small Glaciers. *Remote Sens.* **2025**, *17*, 1486. https://doi.org/10.3390/rs17091486.
8. Žebre, M.; Colucci, R.R.; Giorgi, F.; Glasser, N.F.; Racoviteanu, A.E.; Gobbo, D. 200 years of equilibrium-line altitude variability across the European Alps (1901–2100). *Clim. Dyn.* **2021**, *56*, 1183–1201. https://doi.org/10.1007/s00382-020-05525-7.
9. Ohmura, A.; Boettcher, M. On the Shift of Glacier Equilibrium Line Altitude (ELA) under the Changing Climate. *Water* **2022**, *14*, 2821. https://doi.org/10.3390/w14182821.
10. Italian Glaciological Committee. *Le Campagne Glaciologiche in Italia*; Italian Glaciological Committee: Turin, Italy, 2023.
11. Haeberli, W.; Hoelzle, M. Application of inventory data for estimating characteristics of and regional climate-change effects on mountain glaciers. *Ann. Glaciol.* **1995**, *21*, 206–210.
12. Xue, Y.; Jing, Z.; Kang, S.; He, X.; Li, C. Combining UAV and Landsat data to assess glacier changes on the central Tibetan Plateau. *J. Glaciol.* **2021**, *67*, 862–874. https://doi.org/10.1017/jog.2021.37.
13. Wuite, J.; Nagler, T.; Hetzenecker, M.; Rott, H. Ten years of polar ice velocity mapping using Copernicus Sentinel-1. *Remote Sens. Environ.* **2026**, *332*, 115092. https://doi.org/10.1016/j.rse.2025.115092.
14. Politecnico di Torino. GlacierLAB: Laboratorio Multisito sui Cambiamenti Climatici. 2022. Available online: https://www.diati.polito.it/focus/dipartimento_di_eccellenza_sui_cambiamenti_climatici_2018_2022/laboratorio_multisito/cc_glacier_lab (accessed on 15 January 2026).
15. Berthier, E.; Vincent, C.; Magnússon, E.; Gunnlaugsson, A.Þ.; Pitte, P.; Le Meur, E.; Masiokas, M.; Ruiz, L.; Pálsson, F.; Belart, J.M.C.; et al. Glacier topography and elevation changes derived from Pléiades sub-meter stereo images. *Cryosphere* **2014**, *8*, 2275–2291. https://doi.org/10.5194/tc-8-2275-2014.
16. Rolstad, C.; Haug, T.; Denby, B. Spatially integrated geodetic glacier mass balance and its uncertainty based on geostatistical analysis. *J. Glaciol.* **2009**, *55*, 666–680. https://doi.org/10.3189/002214309789470950.
17. Corte, E.; Ajmar, A.; Camporeale, C.; Cina, A.; Coviello, V.; Tonolo, F.G.; Godio, A.; Macelloni, M.M.; Tamea, S.; Vergnano, A. multi-temporal characterisation of a proglacial system: A multidisciplinary approach. *Earth Syst. Sci. Data* **2024**, *16*, 3283–3306. https://doi.org/10.5194/essd-16-3283-2024.
18. Villa, F.; De Amicis, M.; Maggi, V. GIS analysis of Rutor Glacier (Aosta Valley, Italy) volume and terminus variations. *Geogr. Fis. Din. Quat.* **2007**, *30*, 87–95.
19. Comitato Glaciologico Italiano. Il Ghiacciaio Del Rutor. 2024. Available online: https://glaciologia.it/ghiacciai/il-ghiacciaio-del-rutor/ (accessed on 15 January 2026).
20. Vergnano, A.; Franco, D.; Godio, A. Integrating GPR and ice-thickness models for improved bedrock detection: The case study of Rutor temperate glacier. *Cryosphere* **2025**, *19*, 6965–6988. https://doi.org/10.5194/tc-19-6965-2025.
21. Macelloni, M.M.; Cina, A.; Tonolo, F.G.; Morra di Cella, U. Assessment of the Vertical Accuracy of Satellite-Based Glacier Monitoring: The Rutor Glacier in Italy. In *Geomatics for Environmental Monitoring: From Data to Services. ASITA 2023*; Communications in Computer and Information Science; Springer: Cham, Switzerland, 2024; Volume 2088, pp. 3–15. https://doi.org/10.1007/978-3-031-59925-5_1.
22. Macelloni, M.M.; Corte, E.; Ajmar, A.; Cina, A.; Tonolo, F.G.; Maschio, P.F.; Pisoni, I.N. Multi-platform, Multi-scale and Multi-temporal 4D Glacier Monitoring: The Rutor Glacier Case Study. In *Geomatics for Green and Digital Transition*; Borgogno-Mondino, E., Zamperlin, P., Eds.; Communications in Computer and Information Science; Springer: Cham, Switzerland, 2022; Volume 1651, pp. 1–13. https://doi.org/10.1007/978-3-031-17439-1_29.
23. Ramsey, P.H.; Ramsey, P.P. Optimal Trimming and Outlier Elimination. *J. Mod. Appl. Stat. Methods* **2007**, *6*, 2. https://doi.org/10.22237/jmasm/1193889660.
24. Brasington, J.; Rumsby, B.T.; McVey, R.A. Monitoring and modelling morphological change in a braided gravel-bed river using high resolution GPS-based survey. *Earth Surf. Process. Landforms* **2000**, *25*, 973–990. https://doi.org/10.1002/1096-9837(200008)25:9<973::AID-ESP111>3.0.CO;2-Y.
25. Lane, S.N.; Westaway, R.M.; Hicks, D.M. Estimation of erosion and deposition volumes in a large, gravel-bed, braided river using synoptic remote sensing. *Earth Surf. Process. Landforms* **2003**, *28*, 249–271. https://doi.org/10.1002/esp.483.
26. Wheaton, J.M.; Brasington, J.; Darby, S.E.; Sear, D.A. Accounting for uncertainty in DEMs from repeat topographic surveys: improved sediment budgets. *Earth Surf. Process. Landforms* **2010**, *35*, 136–156. https://doi.org/10.1002/esp.1886.
27. Paul, F.; Bolch, T.; Briggs, K.; et al. Error sources and guidelines for quality assessment of glacier area, elevation change, and velocity products derived from satellite data. *Remote Sens. Environ.* **2017**, *203*, 256–275. https://doi.org/10.1016/j.rse.2017.08.038.
28. Østrem, G.; Stanley, A. *Glacier Mass Balance Measurements: A Manual for Field and Office Work*; Canadian Department of Energy, Mines and Resources, 1969.
29. Nuth, C.; Kääb, A. Co-registration and bias corrections of satellite elevation data sets for quantifying glacier thickness change. *Cryosphere* **2011**, *5*, 271–290. https://doi.org/10.5194/tc-5-271-2011.
30. Agisoft LLC. *Agisoft Metashape User Manual: Professional Edition*; Agisoft LLC: St. Petersburg, Russia, 2023.

31. Hugonnet, R.; McNabb, R.; Berthier, E.; Menounos, B.; Nuth, C.; Girod, L.; Farinotti, D.; Huss, M.; Dussaillant, I.; Brun, F.; et al. Accelerated global glacier mass loss in the early twenty-first century. *Nature* **2021**, *592*, 726–731. https://doi.org/10.1038/s41586-021-03436-z.
32. Fischer, M.; Huss, M.; Hoelzle, M. Surface elevation and mass changes of all Swiss glaciers 1980–2010. *Cryosphere* **2015**, *9*, 525–540. https://doi.org/10.5194/tc-9-525-2015.
33. Bolch, T. Climate change and glacier retreat in northern Tien Shan (Kazakhstan/Kyrgyzstan) using remote sensing data. *Glob. Planet. Change* **2007**, *56*, 1–12. https://doi.org/10.1016/j.gloplacha.2006.07.009.
34. Frey, H.; Huggel, C.; Paul, F.; Haeberli, W. Automated detection of glacier lakes based on remote sensing in view of assessing associated hazard potential. In Proceedings of the 10th International Symposium on High Mountain Remote Sensing Cartography, Kathmandu, Nepal, 8–11 September 2010, pp. 261–272.
35. Haeberli, W.; Hoelzle, M.; Paul, F.; Zemp, M. Integrated monitoring of mountain glaciers as key indicators of global climate change: The European Alps. *Ann. Glaciol.* **2007**, *46*, 150–160. https://doi.org/10.3189/172756407782871512.
36. Ministero dell'Ambiente e della Sicurezza Energetica. Geoportale Nazionale: Servizi Cartografici WMS. Web Map Service (WMS). 2024. Available online: https://gn.mase.gov.it/portale/servizio-di-consultazione-wms (accessed on 15 January 2026).
37. Huss, M. Density assumptions for converting geodetic glacier volume change to mass change. *Cryosphere* **2013**, *7*, 877–887. https://doi.org/10.5194/tc-7-877-2013.
38. Agenzia Regionale per la Protezione dell'Ambiente Valle d'Aosta. 2025. Available online: https://www.arpa.vda.it/notizie/clima/report-annuale-sui-ghiacciai-valdostani-sottozero-dati-2025 (accessed on 15 February 2026).
39. Piermattei, L.; Carturan, L.; Guarnieri, A. Use of terrestrial photogrammetry based on structure-from-motion for mass balance estimation of a small glacier in the Italian Alps. *Earth Surf. Process. Landforms* **2015**, *40*, 1667–1679. https://doi.org/10.1002/esp.3756.
40. Carturan, L.; Filippi, R.; Seppi, R.; Gabrielli, P.; Notarnicola, C.; Bertoldi, L.; Paul, F.; Rastner, P.; Cazorzi, F.; Dinale, R.; et al. Area and volume loss of the glaciers in the Ortles-Cevedale group (Eastern Italian Alps): Controls and imbalance of the remaining glaciers. *Cryosphere* **2013**, *7*, 1339–1359. https://doi.org/10.5194/tc-7-1339-2013.